

Azaquinoid-Based High Spin Open-Shell Conjugated Polymer for n-Type Organic Field-Effect Transistors

Yunseul Kim, Dongseong Yang, Yeon-Ju Kim, Eunhwan Jung, Jong-Jin Park, Yeonsu Choi, Younghyo Kim, Sanjay Mathur, and Dong-Yu Kim*

An open-shell quinoidal conjugated polymer exhibiting n-type semiconducting behavior is successfully synthesized and characterized. An electron-deficient azaaromatic unit is proven to reduce the energy levels of frontier orbitals via the electronegative nitrogen atom and steric hindrance within the polymer backbone. A synthesized azaquinoidal bithiophene (azaQuBT) is a quinoidal bithiophene that is end-functionalized with a pyridine ring. The open-shell quinoidal conjugated polymer, poly(azaquinoidal bithiophene-thiophene), PazaQuBT-T, is synthesized using azaQuBT and thiophene. The extended quinoidal building block, which has an open-shell diradical character, induces low bandgaps, redox amphotericism, and high-spin-induced paramagnetic behavior of the resulting polymer. PazaQuBT-T achieves ambipolar charge-transport behavior in organic field-effect transistor (OFET) devices. Through a PEIE treatment onto the contact electrode, PazaQuBT-based OFETs exhibit unipolar n-channel operation with electron mobility up to $0.98 \text{ cm}^2 \text{ V}^{-1} \text{ s}^{-1}$. This work demonstrates the development of novel open-shell conjugated polymers with high-spin characteristics and n-type semiconducting property.

have attracted attention from researchers because of their structural specificity and unique and noteworthy characteristics such as high electrical charge transport, non-linear optical and magnetic properties, which are uncommon in organic materials.^[3] The quinoid structure is well known for its resonance form of a general aromatic structure, which has a planar structure linked by double bonds between each cyclic ring.^[4] In terms of electronic state, the quinoid structure has a closed-shell form. When the closed-shell quinoid structure is extended, it can be converted into an open-shell diradical structure due to the tendency to recover aromaticity.^[5] These open-shell diradical characteristics of quinoidal compounds could promote interesting spin-induced magnetic behaviors and singlet fission processes.^[6]

Isatin-terminated quinoids have been used to incorporate quinoidal platforms in the conjugated polymer backbone.^[7] Isatin may contain halogen atoms at the 6-position, which allows Pd-catalyzed carbon-carbon cross coupling polymerization (Stille and Suzuki coupling) resulting in para-connected conjugation pathway in the entire polymer backbone. Moreover, isatin-terminated quinoids have crucial advantages because they are easily synthesized via indophenine reactions under ambient conditions and allow easy structural modification. To date, a few isatin-based quinoidal conjugated polymers have been developed by researchers, including our group.^[8] Whereas most quinoidal small molecules have demonstrated n-type field-effect transistor behaviors with strong electron-withdrawing terminal units such as dicyanomethylene groups, conjugated polymers composed of isatin-terminated quinoids rarely exhibit n-type behaviors because of the relatively weak electron-withdrawing nature of the isatin unit.^[9] A conjugated polymer that contained S,S-dioxidized thienoquinoids demonstrated unipolar n-type semiconducting behaviors because of its strong electron withdrawing S=O groups.^[8a,10]


To achieve n-type semiconducting behaviors, azaaromatic compounds may be incorporated into the conjugated building blocks. Azaaromatics contain electronegative nitrogen atoms within the aromatic moieties. They exhibit an electron-deficient nature, easily leading to reductions in the energy levels of frontier orbitals and consequently facilitating easy electron injection.^[11] Moreover, the substitution of carbon with nitrogen affects the alleviation of steric issues between copolymerization counterparts such as thiophene derivatives because of the

1. Introduction

π -Conjugated systems are composed of alternating single and multiple bonds, which have overlapping p-orbitals with delocalized π -electrons in the molecules, leading to attractive features such as optically low bandgaps and electrically semiconducting properties.^[1] These systems have been extensively investigated for promising applications in organic photovoltaics, photo-detectors, thermoelectrics, and organic field-effect transistors (OFETs).^[2] Most π -conjugated platforms, quinoidal compounds,

Y. Kim, D. Yang, Y.-J. Kim,^[†] J.-J. Park,^[††] Y. Choi, Y. Kim, D.-Y. Kim
School of Materials Science and Engineering (SMSE)
Research Institute for Solar and Sustainable Energies (RISE)
Gwangju Institute of Science and Technology (GIST)
Gwangju 61005, Republic of Korea
E-mail: kimdy@gist.ac.kr

E. Jung, S. Mathur
Inorganic and Materials Chemistry
University of Cologne
50939 Cologne, Germany

 The ORCID identification number(s) for the author(s) of this article can be found under <https://doi.org/10.1002/admi.202201205>.

^[†]Present address: Samsung Electronics, Hwaseong-si, Gyeonggi-do, 18448, Republic of Korea

^[††]Present address: LG Chem, Gangseo-gu, Seoul, 07796, Republic of Korea

DOI: 10.1002/admi.202201205

absence of an adjacent proton and non-covalent S–N intramolecular interactions.^[12] Therefore, the polymer could have a coplanar conformation and enhanced π -electron delocalization, leading to efficient charge transport.^[13]

In this study, we designed and synthesized a quinoidal monomer consisting of an electron-deficient pyridine ring. The monomer, azaquinoidal bithiophene (azaQuBT), is characterized compared with a quinoidal bithiophene (QuBT) analogue, which has been reported by our group. AzaQuBT was reacted with a thiophene counterpart via Stille polycondensation, resulting in the successful production of an open-shell quinoidal-aromatic conjugated polymer, identified as poly(azaquinoidal bithiophene-thiophene) (PazaQuBT-T). The replacement of pyridine from the benzene rings leads to better coplanar conformation of the polymer backbone because of the suppression of rotation between the quinoid and thiophene counterparts. The spin characteristics and electronic states of the open-shell quinoidal monomer and polymer were investigated using electron spin resonance (ESR) and Raman spectroscopy. The open-shell quinoidal polymer exhibited a low band gap with broad absorption up to the near-IR region, and amphoteric redox behavior. In OFET devices, PazaQuBT-T demonstrated balanced ambipolar charge transport behaviors in terms of hole and electron mobilities of up to 0.35 and 0.46 cm² V⁻¹ s⁻¹, respectively. Polyethylenimine ethoxylate (PEIE)-treated OFETs based on PazaQuBT-T exhibited unipolar n-channel operation with an electron mobility of ≈ 1.0 cm² V⁻¹ s⁻¹. This study provides the introduction of an extended quinoidal platform into the polymer backbone that allows the development of open-shell conjugated polymers with high-spin characteristics. In addition, we also demonstrate that the replacement of azaaromatics with quinoidal building blocks can achieve *n*-type semiconducting properties.

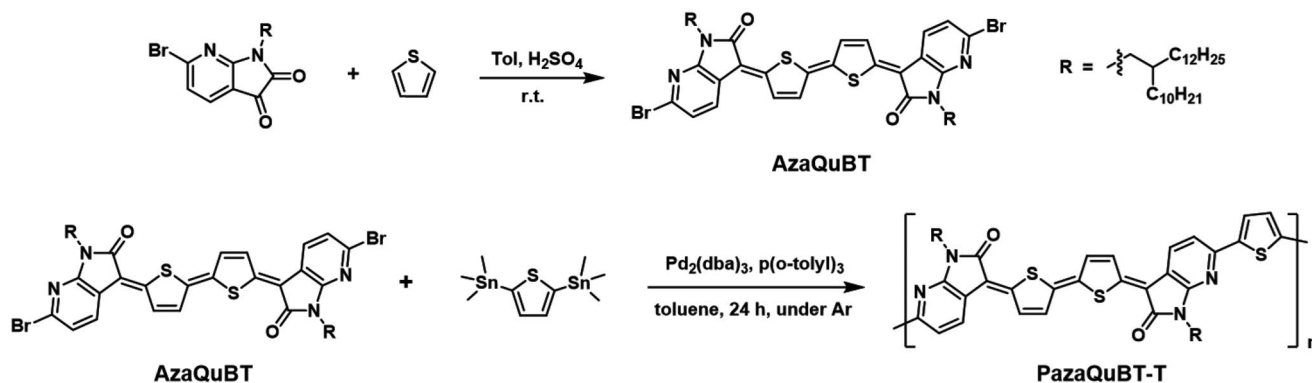
2. Results and Discussion

2.1. Synthesis

Alkylated azaisatin was obtained using a known synthetic method, as shown in Scheme 1.^[14] The alkylated azaisatin was reacted with thiophene under concentrated sulfuric acid, which

is the indophenine reaction as in the method for creating other isatin-terminated quinoids. The reaction mixture was purified by column chromatography, and aza-quinoidal bithiophene (azaQuBT) was obtained as the major product with a yield of $\approx 40\%$. Similar to other isatin-terminated quinoids, azaQuBT could theoretically have six geometric isomers because of double-bond linkages into the quinoidal backbone.^[15] Under ambient conditions, azaQuBT has virtually four geometrical isomers, which are revealed by three spots on the thin-layer chromatography (TLC) plate. As shown in Figure S1 (Supporting Information), azaQuBT is dragged in the TLC plate, a phenomenon that also occurs in column chromatography. Therefore, it was difficult to isolate each isomer via column chromatography, and the geometric structures of the azaQuBT isomers could not be determined. As shown in Figure S2 (Supporting Information), the ¹H-NMR spectrum of azaQuBT exhibited numerous and indistinguishable proton peaks in the aromatic region (δ 7.0–8.6 ppm), indicating that it remains as isomer mixtures under ambient conditions. When the integral of the two protons at the carbon next to the nitrogen atom in the azaisatin is 4, the total integral of protons in the aromatic region is ≈ 8 . AzaQuBT was also characterized via matrix-assisted laser desorption/ionization time-of-flight mass spectrometry (MALDI-TOF-MS), High resolution gas chromatography/mass spectrometry (HRGC/MS) by fast atom bombardment (FAB), and elemental analysis (EA).

PazaQuBT-T was copolymerized via a Stille-coupling reaction between azaQuBT and 2,5-bis(trimethylstannyl)thiophene as an aromatic counterpart (Scheme 1). It was purified via Soxhlet extraction and obtained from the chloroform fraction. The number-average molecular weight (M_n) and polydispersity index (\mathcal{D}) of the polymer were measured to be 31.6 kDa and 3.02, respectively, using high-temperature gel permeation chromatography at 135 °C. The thermal properties of PazaQuBT-T were characterized via thermogravimetric analysis (TGA) and differential scanning calorimetry (DSC), as shown in Figure S5 (Supporting Information). The polymer has excellent thermal stability, with a decomposition temperature (T_d) of 394 °C (5 wt.% loss), as shown in Figure S5a (Supporting Information). In addition, the DSC trace showed no obvious thermal transitions in the 30–280 °C range, indicating that the quinoidal polymer PazaQuBT-T is highly rigid (Figure S5b, Supporting Information).



Scheme 1. Synthetic routes to AzaQuBT and PazaQuBT-T.

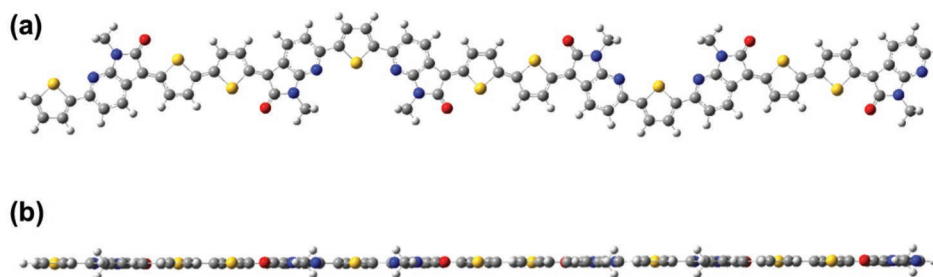


Figure 1. Energy-minimized conformation of a PazaQuBT-T trimer by theoretical calculation. a) Top view and b) side view.

2.2. DFT Calculations

To predict the conformational geometry and frontier molecular orbitals (FMO), density functional theory (DFT) calculations were performed using the Gaussian 09 program at the B3LYP/6-311G (d, p) level. The long alkyl chains were replaced with methyl groups to simplify the calculations. As shown in Figure S6 (Supporting Information), the quinoidal building block, azaQuBT, is highly planar without any torsional angle, similar to QuBT composed of benzene at the end of the molecule. The frontier molecular orbitals of azaQuBT were deeper than those of QuBT (Figure S6b, Supporting Information), which were ascribed to the electron-deficient pyridine ring in the terminal units.^[16] As depicted in **Figure 1** and Figure S7 (Supporting Information), the azaQuBT-T trimer exhibited an extremely planar and linear conformation.^[13a] These results reveal that substitution of a pyridine ring at the end of the quinoidal building block contributes to the elimination of torsional angles between the thiophene counterparts. The highest occupied molecular orbital (HOMO) and lowest unoccupied molecular orbital (LUMO) energy levels are calculated to be -5.04 and -3.71 eV, respectively.

2.3. Spin Characteristics

To investigate the diradical character of the quinoidal monomers and polymer, the diradical character index (γ_0) and singlet-triplet energy gap (ΔE_{S-T}) were quantum chemically calculated. The γ_0 was estimated by the natural orbital occupation numbers obtained by an unrestricted CASSCF calculation. The diradical character of the molecules is quantified by γ_0 . It can have a value between 0 and 1, where a γ_0 value of 0 represents a closed-shell quinoidal structure and a γ_0 value of 1 represents an open-shell diradical structure. The calculated γ_0 and ΔE_{S-T} are listed in Table S1 (Supporting Information). The γ_0 and ΔE_{S-T} were 0.31 and -11.8 kcal mol $^{-1}$ for QuBT analogue, as confirmed by our previous work, and 0.21 and -13.1 kcal mol $^{-1}$ for azaQuBT, respectively. Although azaQuBT showed radical character by open-shell diradical structure due to recover aromaticity into an extended quinoidal platform, the diradical character of azaQuBT is relatively weak than that of QuBT. Interestingly, an azaQuBT-T repeat unit, which is composed of azaQuBT and thiophene counterpart, demonstrated 0.41 of γ_0 value. These results suggest that the PazaQuBT-T polymer composed with azaquinoidal building block and thiophene counterpart may

show high spin characteristics due to increase concentration of radicals in the π -conjugated backbone.^[5c,6g]

Raman spectroscopy, with laser excitation at 532 nm, was performed to investigate the electronic states of the monomers and polymers in the films. In general, carbon-carbon bonds within the conjugated molecules appear in the Raman vibration band in the region of 1300–1700 cm $^{-1}$.^[17] According to the effective conjugation coordinate (ECC) theory, an intense Raman band appears due to the bond-length-alternation (BLA) of a π -conjugated skeleton, corresponding to a collective $\nu(\text{C}=\text{C}/\text{C}-\text{C})$ mode.^[18] To predict Raman vibration, Raman spectra of the azaQuBT and azaQuBT-T dimer were theoretically calculated by DFT calculation at the B3LYP/6-31G+ (d, p) level (Figure S8, Supporting Information). According to simulated Raman spectra, major Raman band of the azaQuBT monomer was revealed at 1462 cm $^{-1}$, which corresponds to collective $\nu(\text{C}=\text{C}/\text{C}-\text{C})$ stretching mode (see eigenvectors in Figure S9, Supporting Information). In addition, major Raman bands of the azaQuBT-T dimer were observed in 1434 and 1411 cm $^{-1}$; the former corresponds to collective $\nu(\text{C}=\text{C}/\text{C}-\text{C})$ stretching mode and the latter corresponds to the $\nu(\text{C}=\text{C})$ stretching mode within the thiophene aromatic counterpart. Interestingly, azaQuBT monomer and azaQuBT-T dimer exhibited a characteristic Raman band at 1546 and 1537 cm $^{-1}$, respectively, which corresponds to $\nu(\text{C}=\text{C}/\text{C}-\text{C})$ stretching mode at 3-position in the azaisatin. As shown in Figure S10 (Supporting Information), azaQuBT monomer have highest spin density at the 3-position in the azaisatin. Therefore, when open-shell structure is more formed within the azaQuBT, a characteristic Raman band at ≈ 1540 cm $^{-1}$ would be more intense.

As shown in Figure S11 (Supporting Information), azaQuBT exhibited a collective $\nu(\text{C}=\text{C}/\text{C}-\text{C})$ Raman band at 1443 cm $^{-1}$, which is the same value as that of QuBT. Moreover, for azaQuBT, an additional Raman band appeared at 1551 cm $^{-1}$, which is ascribed to the open-shell diradical due to gained aromaticity.^[5c] In **Figure 2a**, the collective Raman band of PazaQuBT-T downshifted to 1423 cm $^{-1}$ compared to that of the azaQuBT monomer because of the extended π -electron delocalization in the conjugated backbone. Interestingly, the characteristic Raman peak appeared at 1550 cm $^{-1}$, corresponding to the stretching mode of the open-shell diradical form. This Raman band became much stronger and slightly downshifted compared to that for the azaQuBT monomer, indicating an extended effective conjugated length and a large amount of open-shell diradicals in PazaQuBT-T.

To evaluate the radical characteristics of the open-shell monomer and polymer at the room temperature, X-band ESR

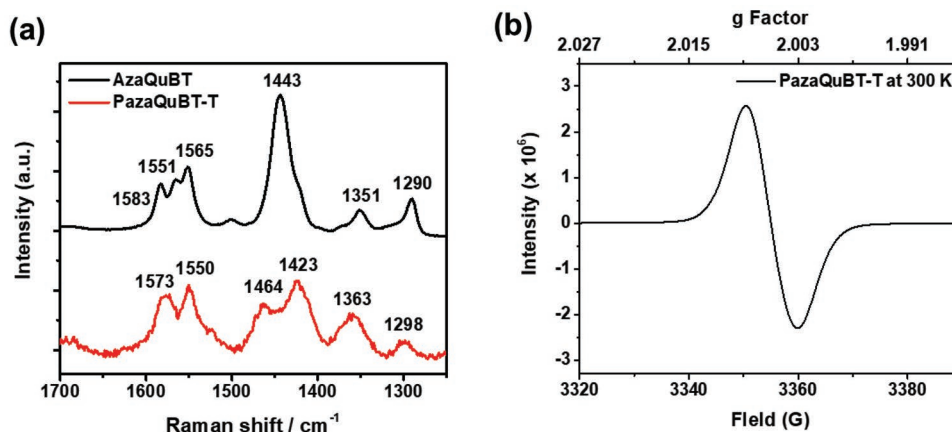


Figure 2. a) Resonant Raman spectra of azaQuBT and PazaQuBT-T films at 532 nm laser. b) Electron spin resonance (ESR) spectrum of PazaQuBT-T in powder.

measurements were performed in the solid state at 300 K. Both the azaquinoidal monomer and polymer revealed a single ESR signal at $g \approx 2.005$, larger than that of the carbon-centered radicals, which had a g value of ≈ 2.003 , as shown in Figure S12 (Supporting Information) and Figure 2b.^[19] The nitrogen atom at the azaisatin termini affected π -type carbon-centered radicals delocalized within the conjugated backbone, leading to an increase in the g -factor.^[20] The monomer azaQuBT exhibited a broad and single ESR signal with a weak shoulder peak. This indicates that azaQuBT has an open-shell diradical form at room temperature, and that the π -type carbon-centered radicals generated at the end of the quinoids are affected by nitrogen atoms. As shown in Figure 2b, PazaQuBT-T composed of azaQuBT units exhibited a very intense single ESR signal. This indicates that the polymer contains large amounts of open-shell radicals within the polymer backbone, which agree well with the results of DFT calculation and Raman analysis. A previously reported aromatic-quinoid conjugated polymer, PQuBT-TV, which contains a quinoidal platform of the same length, also exhibited a strong spin character. In addition, variable temperature ESR (VT-ESR) measurements were carried out to identify the spin state of radicals at the ground state. As shown in Figure S13 (Supporting Information), both azaquinoid-based monomer and polymer exhibited gradually increased ESR signal with temperature. These results indicate that both have thermally populated triplet state.^[21] We demonstrated that, for isatin-terminated quinoids, direct introduction of a longer thienoquinoid ring into the conjugated polymer backbone is an effective strategy for developing high-spin open-shell conjugated polymers.^[5c]

2.4. Electrochemical and Optical Properties

The electronic energy levels were obtained via cyclic voltammetry (CV) using ferrocene as a reference, and measurements were performed on quinoidal monomers and a polymer in solution and film, respectively. The energy levels of HOMO and LUMO were estimated from the onsets for the first oxidation and reduction potentials, respectively (Table 1). As shown in Figure S14 (Supporting Information), the oxidation and reduction potentials

of azaQuBT were higher than those of QuBT. This indicates that azaQuBT has lower HOMO and LUMO energy levels compared to those of QuBT; the HOMO/LUMO energy levels are $-5.22/-3.84$ eV for QuBT and $-5.33/-3.94$ eV for azaQuBT. These results corroborate the DFT calculations, according to which electron-deficient pyridine rings in azaQuBT induce deeper FMO energy levels.^[22] PazaQuBT-T also exhibited reversible oxidation and reduction peaks, which reflect a quinoidal character that enabled the formation of stable radical anions and/or cations. (Figure 3a). Its HOMO and LUMO energy levels are -5.03 and -3.74 eV, respectively. These energy levels are higher than those of the corresponding azaQuBT monomer, which is attributed to the electron-donating thiophene counterpart in the polymer backbone. The electrochemical band gap is reduced to 1.29 eV compared to that of azaQuBT (1.39 eV). This result suggests that the replacement of pyridine rings at the end of the quinoid induced a well-delocalized polymer backbone because of the reduced torsional angles with the thiophene counterpart, which is consistent with the DFT calculation. Interestingly, the first reduction signal exhibits excellent reversibility, which is probably due to the high stability of the radical anion in the azaquinoid building block.^[23]

UV-vis-NIR absorption measurements were performed to investigate the optical properties of PazaQuBT-T. As shown in Figure 3b, PazaQuBT-T exhibited a broad absorption up to the near-IR region and a narrow optical bandgap of 1.13 eV due to small bond-length-alternation and extending π -electron delocalization of the azaQuBT building block. The absorption spectrum in solution showed two noticeable absorption maximum peaks, which corresponded to a 0–1 transition peak at 845 nm and a 0–0 transition peak at 967 nm. These two transition peaks are attributed to H - and J -type aggregates; the former

Table 1. Optical and electrochemical properties of PazaQuBT-T.

	Solution		Film		HOMO [eV] ^{a)}	LUMO [eV] ^{a)}	E_g^{CV} [eV] ^{a)}
	λ_{max} [nm]	E_g^{opt} [eV]	λ_{max} [nm]	E_g^{opt} [eV]			
PazaQuBT-T	845, 967	1.13	813, 981	1.11	-5.03	3.74	1.29

^{a)} Determined by CV. $E_{HOMO/LUMO} = -4.8 - (E_{[onset, ox]}/E_{[onset, red]} - E_{1/2}(\text{ferrocene}))$ (eV).

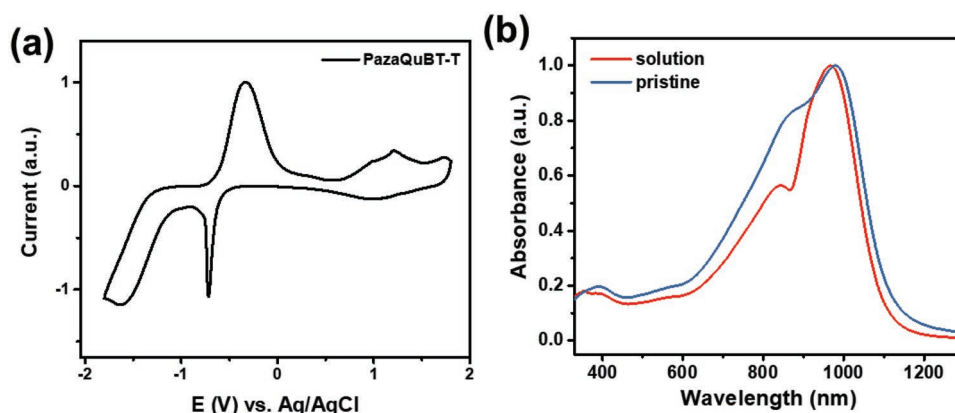


Figure 3. a) Cyclic voltammogram (CV) in a film and b) UV-vis-NIR absorption spectra in solution and film of PazaQuBT-T.

corresponds to 0–1 transition peak in the longer wavelength region and the latter corresponds to 0–0 transition peak in the shorter wavelength region. The azaQuBT unit is extremely planar owing to its quinoidal structure; therefore, it is favorable for stacking with *H*-type aggregates.^[5c,15] The polymer film exhibited an enhanced 0–1 transition peak compared to the polymer solution, indicating that the polymer chains prefer to form *H*-type aggregates in the thin film state.^[24] Meanwhile, the PazaQuBT-T film exhibited a broader absorption range and slightly red-shifted absorption maximum peak compared to those of the solution.

2.5. Microstructural Analysis

The molecular packing and structural order information of PazaQuBT-T were investigated via 2D grazing incidence wide-angle X-ray scattering (2D-GIWAXS). The 2D-GIWAXS images are shown in **Figure 4a**, and their in-plane and out-of-plane profiles are shown in **Figure 4b** and **Figure S15** (Supporting Information), respectively. The 2D-GIWAXS parameters are listed in Table S2 (Supporting Information). The pristine film exhibited only a weak (100) diffraction peak in the in-plane direction, corresponding to lamellar stacking. However, the PazaQuBT-T in the annealed film adopts a bimodal arrangement on the surface,

which is indication of co-existing edge-on and face-on arrangements. Higher-order (*h*00) peaks were observed in the in-plane direction, with a *d*-spacing of 26.4 Å. In addition, (010) diffraction peaks appeared in both the in- and out-of-plane directions with a *d*-spacing of ≈3.5 Å. These (010) peaks are ascribed to π - π stacking, suggesting that highly planar quinoids could induce strong intermolecular interactions. This result indicates that the post-thermal treatment enhances structural ordering and crystallinity. The surface morphology of the PazaQuBT-T films was confirmed using atomic force microscopy (AFM) images (**Figure S16**, Supporting Information). The AFM height images revealed that both the pristine and annealed films have smooth surface topographies with root-mean-square (RMS) roughness values of 0.379 nm and 0.449, respectively. The RMS roughness increased slightly with thermal annealing. These observations indicate that thermal treatment improves the crystallinity, which is consistent with the 2D-GIWAXS analysis.

2.6. OFET Devices

OFET devices with top-gate/bottom-contact (TG/BC) configurations were fabricated to evaluate the charge transport properties of PazaQuBT-T. Polymer films were prepared via spin coating using a 10 mg mL⁻¹ solution in *o*-dichlorobenzene,

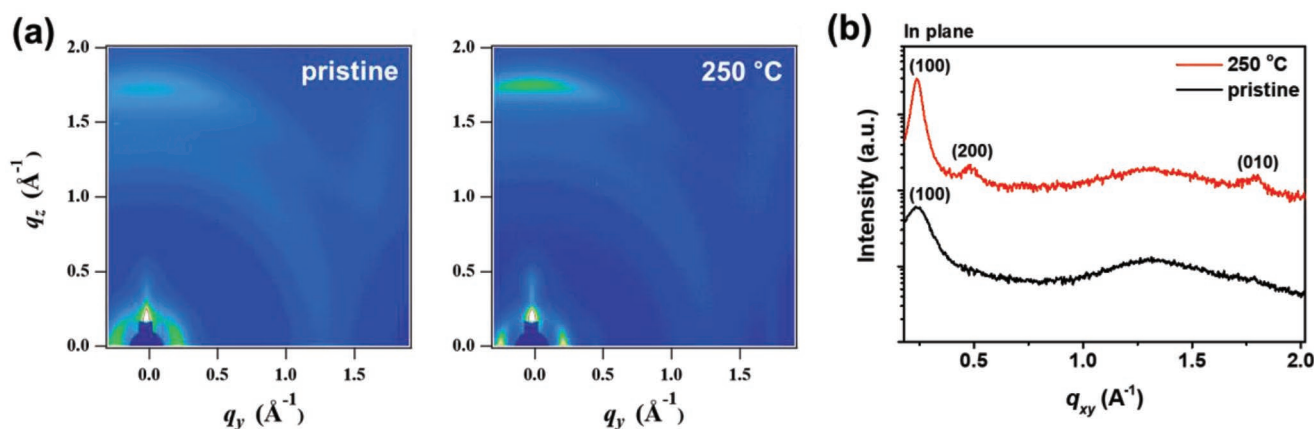


Figure 4. a) 2D-GIWAXS patterns of PazaQuBT-T of film in pristine and annealed at 250 °C, and corresponding line-cut in b) in-plane direction.

Table 2. Device performance parameters of the OFET devices based on PazaQuBT-T films in pristine and annealed at 250 °C.

Ann. Condition	Hole			Electron		
	μ_{avg} [μ_{max}] [cm ² V ⁻¹ s ⁻¹]	V_{th} [V]	I_{on}/I_{off} ratio	μ_{avg} [μ_{max}] [cm ² V ⁻¹ s ⁻¹]	V_{th} [V]	I_{on}/I_{off} ratio
w/o	$9.87 \times 10^{-3} \pm 2.30 \times 10^{-4}$	-15.4 ± 1.7	10^3	$1.09 \times 10^{-2} \pm 2.58 \times 10^{-3}$	22.4 ± 1.7	10^3
250 °C	0.29 ± 0.03 (0.35)	-40.0 ± 1.2	10^0	0.41 ± 0.04 (0.46)	31.5 ± 2.9	10^1
250 °C ^{a)}	—	—	—	0.64 ± 0.19 (0.98)	26.7 ± 1.4	10^2

^{a)}Treated with 0.4 wt.% PEIE.

as detailed in the Supporting Information. The output and transfer curves of the OFET devices are shown in Figure S17 (Supporting Information), and the performance parameters are listed in Table 2. PazaQuBT-T exhibited a fairly balanced ambipolar operation in the OFETs. The OFET device constructed using pristine films exhibited relatively low hole and electron mobilities of 9.87×10^{-3} and 1.09×10^{-2} cm² V⁻¹ s⁻¹, respectively. After thermal annealing at 250 °C, the best performance was achieved, in terms of hole and electron mobilities of 0.35 and 0.46 cm² V⁻¹ s⁻¹, respectively. As mentioned in the morphological characterization, thermal annealing affects the higher molecular packing and crystallinity of the film, leading to an improvement in the charge carrier mobility of OFET devices. Unfortunately, all OFET devices exhibited low I_{on}/I_{off} ratios, which could be attributed to a high off current due to rich radicals within the open-shell polymer backbone.

To produce unipolar n-type OFET devices, a thin PEIE layer was coated onto the bottom-contact substrate with a Ni/Au source and drain electrodes. The work function of Au can be lowered by amine groups in the PEIE, which aids electron injection.^[25] The PEIE deposition condition was optimized via screening of the concentration of the PEIE solution in 2-methoxyethanol. The best concentration was determined to be 0.04 wt.%. The representative transfer curves of the optimized OFET devices are shown in Figure 5a, and the device parameters are listed in Table 2. The PEIE-treated OFETs exhibited unipolar n-channel operation with improved mobility compared to those of the OFETs constructed using neat films without PEIE, suggesting that the PEIE treatment is effective for injecting electrons and blocking holes. The best electron mobility among the tested devices is 0.98 cm² V⁻¹ s⁻¹, which is two times higher than that obtained using a neat PazaQuBT-T film. Moreover, the PEIE-treated OFET device demonstrated a decreased threshold voltage (V_{th}) and an increased I_{on}/I_{off} ratio. The improvement in the OFET characteristics is due to reduced contact resistance for electron injection, by applying the PEIE treatment. To further investigate the effect of the PEIE treatment, the contact resistance (R_c) was evaluated using the Y-function method (Figure 5b).^[26] The contact resistance values for the untreated and PEIE-treated OFET devices are 440 and 310 k Ω , respectively. This result indicates that the contact resistance for the electron injection was successfully reduced by the PEIE treatment, leading to improved electron mobility and diminished threshold voltage in PazaQuBT-T-based OFETs.

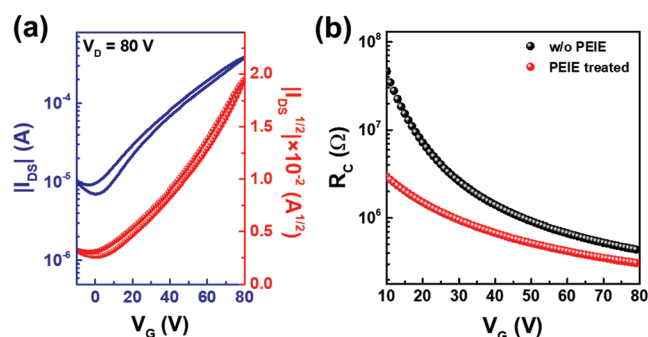


Figure 5. a) Representative transfer curves of optimized OFET devices based on annealed film with 0.4 wt.% PEIE. b) R_c as function of the gate voltage of PazaQuBT-T neat based- and PEIE-treated OFET devices.

3. Conclusions

A new quinoidal building block comprising electron-deficient pyridine rings was designed and synthesized via a simple indophenine reaction. This building block is identified to be azaQuBT. The azaQuBT monomer exhibited deeper HOMO and LUMO energy levels compared to those of the QuBT analogue because of the electron-withdrawing ability of the pyridine rings. Moreover, the azaQuBT with an extended quinoid structure was ESR-active, indicating an open-shell diradical nature due to its gain in aromaticity. The open-shell quinoidal-aromatic conjugated polymer, PazaQuBT-T, was synthesized via a Stille-coupling reaction. PazaQuBT-T demonstrated more intense open-shell characteristics and a stronger ESR signal at room temperature than those of the corresponding azaQuBT building block. This finding indicates that PazaQuBT-T possesses large amounts of stable radicals along the polymer backbone, leading to high-spin characteristics that are uncommon in organic materials. The polymer exhibited broad absorption of up to 1200 nm and a low band gap due to the extended quinoidal building blocks. OFET devices fabricated with PazaQuBT exhibit balanced ambipolar charge-transport behaviors, resulting from the substitution of electron-deficient pyridine rings. OFET performance was improved when the contact Au electrodes of the devices were subjected to PEIE treatment. The PEIE-treated OFET devices demonstrated unipolar n-channel operation with electron mobility of up to 0.98 cm² V⁻¹ s⁻¹. In summary, this study provides an effective molecular design strategy for high-spin open-shell conjugated polymers based on a quinoidal platform, and demonstrates the development of n-type semiconducting materials via structural modification using electron-deficient azaaromatics. Furthermore, the open-shell organic semiconductors based on quinoidal platforms could allow organic-based spin-related applications beyond the field of organic electronics.

4. Experimental Section

Materials and Methods: All chemical reagents were purchased and used as received. Thin layer chromatography (TLC) was performed on silica gel-coated glass sheets. Gas chromatography-mass spectrometry (GC-MS) was used to obtain mass data using a PerkinElmer Clarus 690 combined with a PerkinElmer Clarus SQ 8 T. ¹H-NMR spectra and ¹³C-NMR were recorded on a Jeol 400 MHz (JNM-EX400) and

600 MHz Bruker Advance Neo spectrometers using CDCl_3 as the solvent. Chemical shifts were reported as δ values (ppm) relative to internal tetramethylsilane (TMS). Matrix-assisted laser desorption/ionization time-of-flight mass spectrometry (MALDI-TOF-MS) analysis was carried out on an AXIMA Assurance (Shimadzu) with α -cyano-4-hydroxycinnamic acid as the matrix. High resolution gas chromatography/mass spectrometry (HRGC/MS) by fast atom bombardment (FAB) analysis was performed on a JEOL JMS-700 spectrometer with 3-nitrobenzyl alcohol as the matrix. Elemental analysis (EA) was performed using a UNICUBE (Elementar). The number-average molecular weight (M_n) and polydispersity index (\bar{D}) were determined by an Agilent Technologies PL-GPC220 series gel permeation chromatography (GPC) with 1,2,4-trichlorobenzene as the eluent at 135 °C. The data was calibrated against polystyrene standards with narrow-polydispersity. Thermogravimetric analysis (TGA) was carried out on a SDT Q600 (Waters) at a rate of 10 °C min⁻¹ under nitrogen atmosphere. Differential scanning calorimetry (DSC) was performed on a Q20 instrument (TA instruments) at a heating rate of 10 °C min⁻¹ under nitrogen atmosphere. X-band electron spin resonance (ESR) spectra were acquired using a Bruker EMXplus-9.5/2.7 spectrometer at a microwave frequency of 9.427 GHz. Ultraviolet-visible-near infrared (UV-Vis-NIR) absorption spectra were collected on 500 PC UV/Vis/NIR spectrophotometer (PerkinElmer). Cyclic voltammetry (CV) measurement was performed using an Eco Chemie Autolab PGSTAT30 instrument with a three-electrode cell. The supporting electrolyte was a degassed 0.1 M tetra-n-butylammonium hexafluorophosphate (n-Bu₄NPF₆)/CH₂Cl₂ solution for solution and 0.1 M n-Bu₄NPF₆/CH₃CN solution for film state, respectively. The testing was conducted at a scan rate of 50 mV s⁻¹. A gold electrode and an indium tin oxide coated with the polymer films were used as the working electrode for solution and film state, respectively. A platinum wire and an Ag/AgCl electrode were used as counter and reference electrodes, respectively. A 0.1 M ferrocene solution was used for calibration of CV measurements. The half-wave potential of ferrocene ($E_{1/2}(\text{ferrocene})$) was found to be 0.496 and 0.483 V for solution and film state, respectively, related to the Ag/Ag⁺ reference electrode. DFT calculation was conducted to optimize the frontier molecular orbitals and molecular geometry at the B3LYP/6-311+G (d, p) level using Gaussian 16 software. In addition, DFT calculation was performed to predict Raman vibration using the B3LYP/6-31+G (d, p) level using Gaussian 16 software. Theoretical frequencies were scaled uniformly by a scale factor of 0.964. Raman spectra were obtained using an Andor Shamrock SR-500i-A spectrometer (Andor Tech) equipped with a charge-coupled device (DDC) camera (DV420A-OE, Andor Tech). A 532 nm laser (SCL-532 = 200T, Shanghai Dream Lasers Technology Co., Ltd) was explored. Atomic force microscopy (AFM) was performed in the tapping mode using a Nanoscopy V Multimode 8 instrument. 2D-grazing incidence wide-angle X-ray scattering (2D-GIWAXS) measurements were performed using the synchrotron radiation source 3C beamline at the Pohang Accelerator Laboratory (PAL).

Synthesis of 2-Decyltetradecyl-6-Bromo-7-Azaindole (1): 6-Bromo-7-azaindole (2.0 g, 10.15 mmol) was dissolved in dry DMF (10 mL) in one-neck flask. Sodium hydride (400 mg, 60% in mineral oil) was dissolved in dry DMF at room temperature and stirred for 10 min. 6-Bromo-7-azaindole solution was slowly added to sodium hydride solution in ice bath and stirred for 45 min. After removing the ice bath, 2-decyltetradecyl bromide (5.51 g, 13.20 mmol) was added slowly to solution mixture, which was stirred overnight. The reaction mixture was poured into water until no obvious bubble, extracted with ethyl acetate for two times. The combined organic layers were dried with anhydrous MgSO₄, concentrated under reduced pressure. The crude was purified with silica-gel chromatography with hexane and then dichloromethane:hexane (1:10, v/v) to afford a colorless oil (3.79 g, yield: 70%). ¹H NMR (400 MHz, 1,1,2,2-tetrachloroethane-d₂) δ 7.75 (d, J = 8.2 Hz, 1H), 7.21–7.14 (m, 2H), 6.45 (d, J = 3.6 Hz, 1H), 4.14 (d, J = 7.0 Hz, 2H), 1.94 (s, 1H), 1.23–1.17 (m, 40H), 0.89 (t, J = 6.7 Hz, 6H). MS (GC, EI, m/z): [M]⁺ calcd for C₃₁H₅₁BrN₂: 533.34; found: 533.00.

Synthesis of 2-Decyltetradecyl-6-Bromo-7-Azaisatin (2): To a two-neck round flask equipped with a magnetic stir bar was added pyridinium

chlorochromate (PCC) (1.51 g, 7.03 mmol) and silica gel (1.51 g). The flask was purged with argon and added anhydrous 1,2-dichloroethane (12 mL) and acetonitrile (18 mL). A solution of compound 1 (1.50 g, 2.81 mmol) in 1,2-dichloroethane (6 mL) was added to the reaction mixture, which was stirred at room temperature. An aluminum chloride (37.50 mg, 0.28 mmol) was added, and the mixture was heated at 80 °C for 3 h. The reaction mixture was allowed to cool to room temperature. The mixture was transferred to a separatory funnel, and an organic layer was extracted with hexane. The organic layer was concentrated in vacuo and subjected to flash column chromatography (SiO₂, hexane:toluene = 8:1 (v/v) to hexane:ethyl acetate = 9:1 (v/v) to afford 2-decyltetradecyl-6-bromo-7-azaisatin (0.98 g, 1.74 mmol) in a yield of 62% as an orange solid. ¹H NMR (400 MHz, CD₂Cl₂): δ 7.64 (d, J = 7.7 Hz, 1H), 7.28 (d, J = 7.7 Hz, 1H), 3.69 (d, J = 7.2 Hz, 2H), 1.97 (m, 1H), 1.23–1.17 (m, 40H), 0.88 (t, J = 6.9 Hz, 7H); ¹³C NMR (101 MHz, CD₂Cl₂) δ 181.12, 164.58, 158.57, 149.91, 133.97, 123.26, 110.39, 43.69, 36.17, 32.00, 31.99, 31.41, 29.97, 29.76, 29.75, 29.72, 29.71, 29.69, 29.68, 29.43, 29.42, 26.17, 22.76, 13.95; MS (GC, EI, m/z): [M+2H]²⁺ calcd for C₃₁H₅₁BrN₂O₂: 565.32; found: 565.00.

Synthesis of Azaquinoidal Bithiophene (azaQuBT) (3): To a 50 mL round flask equipped with a magnetic stir bar was added thiophene (0.39 g, 4.26 mmol) and compound 2 (1.20 g, 2.13 mmol) in toluene of 15 mL, and the mixture was stirred at room temperature. Concentrated sulfuric acid (0.1 mL) was added dropwise to the solution mixture, which was stirred at room temperature for 3 h. The reaction mixture was extracted with chloroform, and the combined organic layers were dried over MgSO₄. After removal of the solvent under reduced pressure, the crude was purified by column chromatography (SiO₂, hex: EA = 4:1 (v/v)) to afford azaquinoidal bithiophene (1.01 g, yield: 38%) as a blue solid. MS (MALDI-TOF-MS, CHCl₃): [M+H]⁺ calcd for C₇₀H₁₀₆Br₂N₄O₂S₂, 1260.57; found, 1260.40; HR-MS (FAB, m/z): [M+H]⁺ calcd for C₇₀H₁₀₆Br₂N₄O₂S₂, 1258.6103, found, 1258.6202; EA: calcd for C₇₀H₁₀₆Br₂N₄O₂S₂: C, 66.75; H, 8.48; N, 4.45; O, 2.54; S, 5.09; found: C, 67.36; H, 8.597; N, 4.39; O, 3.063; S, 5.148.

Synthesis of Poly(Azaquinoidal Bithiophene-Thiophene) (PazaQuBT-T): Compound 3 (503.83 mg, 0.4 mmol) and 2,5-bis(trimethylstannyl) thiophene (163.90 mg, 0.4 mmol), Pd₂(dba)₃ (7.33 mg, 2 mol%) and P(o-tolyl)₃ (9.74 mg, 8 mol%) were added with anhydrous toluene (12 mL) into a two-neck round flask. The reaction mixture was stirred and heated for 24 h at 110 °C under argon atmosphere, and then cooled to room temperature. The crude polymer was precipitated in methanol: HCl (1:1, v/v) and purified by Soxhlet extraction with methanol, acetone, hexane, and chloroform. The chloroform fraction was collected and reduced in vacuo, and then the polymer was filtered and dried, affording PazaQuBT-T (250 mg, yield: 53%). GPC: M_n = 31.6 kDa, \bar{D} = 3.02.

DFT Calculation for Diradical Characteristics: The singlet and triplet open-shell structures were simulated using DFT calculations, which are conducted in the gas phase using the Gaussian 16 A.03 software package. Geometry optimization and frequency simulation were performed by DFT calculations using the functional (U)B3LYP with the 6-311G (d, p) basis set. The singlet-triplet energy gap (ΔE_{S-T}) in the open-shell system was carried out under the same level of theory, where $\Delta E_{S-T} = E_S - E_T$. The diradical character index (y_0) were calculated based on the CASSCF(6,6)/6-31G level with NBO analysis and was described by the following equations

$$y_0 = \frac{(1-T)^2}{(1+T^2)} \quad (1)$$

$$T = \frac{(n_{\text{HONO}} - n_{\text{LUNO}})}{2} \quad (2)$$

where T is the orbital overlap between the corresponding orbital pairs (calculated by the occupation numbers of natural orbitals) and n_{HONO} and n_{LUNO} are the occupation numbers of the highest occupied and lowest unoccupied natural orbitals, respectively.

Device Fabrication: Top-gate/bottom-contact (TG/BC) field-effect transistors with Au and Ni (15 and 3 nm thick) source and drain contacts was prepared with a lift-off photolithography onto Corning Eagle 2000 glass

substrates. The channel length (L) and channel width (W) were 20 μm and 1.0 mm, respectively. The patterned substrates were successively cleaned in an ultrasonicator with DI water, acetone, and iso-propanol for 10 min each, and treated with UV/ozone for 30 min. The polymer was dissolved in anhydrous ortho-dichlorobenzene (o-DCB) to produce a 10 mg mL⁻¹ solution. Spin-coating was done using the polymer solution onto the glass substrates at 1500 rpm for 1 min. After deposition of the organic layer, the films were annealed at 250 °C for 20 min. The dielectric layer was formed by spin-coating using poly(methyl methacrylate) (PMMA, Aldrich) to obtain a 500 nm thick layer, which was baked at 80 °C for 2 h. An aluminum top-gate electrode (50 nm thick) was finally evaporated with a shadow mask to produce the final device. The transistor characteristics were measured by a Keithley 4200-SCS instrument. Fabrication and electrical testing were carried out in a nitrogen-filled glovebox.

Supporting Information

Supporting Information is available from the Wiley Online Library or from the author.

Acknowledgements

This work was supported by the National Research Foundation of Korea (NRF) grant funded by the Korea government (NRF-2021R1A2B5B03086824) and Samsung Research Funding & Incubation Center of Samsung Electronics under Project Number SRFC-MA1802-03. The authors acknowledge the Korea Basic Science Institute (KBSI) for providing the AFM measurement and the Pohang Accelerator Laboratory for providing a synchrotron radiation source at the 9A beamline to measure the 2D-GIWAXS used in this study. Y.K. contributed to all the experimental work and analysis. D.Y. and Y.-J.K. performed the fabrication and measurement of OFET devices. E.J. and S.M. performed the DFT simulation and discussed the related data. J.-J.P. and Y.C. contributed to discussion for this study. Y.K. conducted the purification of monomer and contributed to discussion. Y.K. and D.-Y.K. wrote this manuscript. All authors commented on the paper.

Conflict of Interest

The authors declare no conflict of interest.

Data Availability Statement

The data that support the findings of this study are available on request from the corresponding author. The data are not publicly available due to privacy or ethical restrictions.

Keywords

high-spin characteristics, open-shell conjugated polymers, open-shell quinoidal conjugated polymers, organic field-effect transistors

Received: May 31, 2022
Revised: August 26, 2022
Published online:

- [1] a) C. Wang, H. Dong, W. Hu, Y. Liu, D. Zhu, *Chem. Rev.* **2012**, 112, 2208; b) T. M. Swager, *Macromolecules* **2017**, 50, 4867.

- [2] a) C. Liu, K. Wang, X. Gong, A. J. Heeger, *Chem. Soc. Rev.* **2016**, 45, 4825; b) D. Yang, D. Ma, *Adv. Opt. Mater.* **2019**, 7, 1800522; c) H. Bronstein, C. B. Nielsen, B. C. Schroeder, I. McCulloch, *Nat. Rev. Chem.* **2020**, 4, 66.
[3] a) J. Casado, R. P. Ortiz, J. T. López Navarrete, *Chem. Soc. Rev.* **2012**, 41, 5672; b) T. Kubo, *Chem. Lett.* **2014**, 44, 111.
[4] J. Huang, G. Yu, *Mater. Chem. Front.* **2021**, 5, 76.
[5] a) Z. Zeng, X. Shi, C. Chi, J. T. López Navarrete, J. Casado, J. Wu, *Chem. Soc. Rev.* **2015**, 44, 6578; b) D. Yuan, D. Huang, S. M. Rivero, A. Carreras, C. Zhang, Y. Zou, X. Jiao, C. R. McNeill, X. Zhu, C.-a. Di, D. Zhu, D. Casanova, J. Casado, *Chem* **2019**, 5, 964; c) Y. Kim, Y.-J. Kim, Y.-A. Kim, E. Jung, Y. Mok, K. Kim, H. Hwang, J.-J. Park, M.-G. Kim, S. Mathur, D.-Y. Kim, *ACS Appl. Mater. Interfaces* **2021**, 13, 2887.
[6] a) A. E. London, H. Chen, M. A. Sabuj, J. Tropp, M. Saghayezhian, N. Eedugurala, B. A. Zhang, Y. Liu, X. Gu, B. M. Wong, N. Rai, M. K. Bowman, J. D. Azoulay, *Sci. Adv.* **2019**, 5, eaav2336; b) T. L. D. Tam, C. K. Ng, S. L. Lim, E. Yildirim, J. Ko, W. L. Leong, S.-W. Yang, J. Xu, *Chem. Mater.* **2019**, 31, 8543; c) T. L. D. Tam, G. Wu, S. W. Chien, S. F. V. Lim, S.-W. Yang, J. Xu, *ACS Mater. Lett.* **2020**, 2, 147; d) L. Wang, X. Liu, X. Shi, C. L. Anderson, L. M. Klivansky, Y. Liu, Y. Wu, J. Chen, J. Yao, H. Fu, *J. Am. Chem. Soc.* **2020**, 142, 17892; e) S. Dong, Z. Li, *J. Mater. Chem. C* **2022**, 10, 2431; f) D. J. Adams, K. S. Mayer, M. Steelman, J. D. Azoulay, *J. Phys. Chem. C* **2022**, 126, 5701; g) X.-X. Chen, J.-T. Li, Y.-H. Fang, X.-Y. Deng, X.-Q. Wang, G. Liu, Y. Wang, X. Gu, S.-D. Jiang, T. Lei, *Nat. Commun.* **2022**, 13, 2258.
[7] T. Mikie, I. Osaka, *J. Mater. Chem. C* **2020**, 8, 14262.
[8] a) Y. Deng, B. Sun, Y. He, J. Quinn, C. Guo, Y. Li, *Angew. Chem., Int. Ed.* **2016**, 55, 3459; b) Y. Kim, H. Hwang, N.-K. Kim, K. Hwang, J.-J. Park, G.-I. Shin, D.-Y. Kim, *Adv. Mater.* **2018**, 30, 1706557; c) Y. Sun, Y. Zhang, Y. Ran, L. Shi, Q. Zhang, J. Chen, Q. Li, Y. Guo, Y. Liu, *J. Mater. Chem. C* **2020**, 8, 15168; d) K. Hwang, M.-H. Lee, J. Kim, Y.-J. Kim, Y. Kim, H. Hwang, I.-B. Kim, D.-Y. Kim, *Macromolecules* **2020**, 53, 1977; e) X. Zhao, H. Cai, Y. Deng, Y. Jiang, Z. Wang, Y. Shi, Y. Han, Y. Geng, *Macromolecules* **2021**, 54, 3498.
[9] C. Zhang, X. Zhu, *Adv. Funct. Mater.* **2020**, 30, 2000765.
[10] K. Guo, B. Wu, Y. Jiang, Z. Wang, Z. Liang, Y. Li, Y. Deng, Y. Geng, *J. Mater. Chem. C* **2019**, 7, 10352.
[11] a) T. L. D. Tam, T. T. Lin, *Macromolecules* **2016**, 49, 1648; b) Y.-Z. Dai, N. Ai, Y. Lu, Y.-Q. Zheng, J.-H. Dou, K. Shi, T. Lei, J.-Y. Wang, J. Pei, *Chem. Sci.* **2016**, 7, 5753; c) Y. Wang, T. Hasegawa, H. Matsumoto, T. Mori, T. Michinobu, *Adv. Mater.* **2018**, 30, 1707164.
[12] a) N. E. Jackson, B. M. Savoie, K. L. Kohlstedt, M. Olvera de la Cruz, G. C. Schatz, L. X. Chen, M. A. Ratner, *J. Am. Chem. Soc.* **2013**, 135, 10475; b) Q. Zhang, J. Huang, K. Wang, W. Huang, *Adv. Mater.* **2022**, n/a, 2110639.
[13] a) J. Huang, Z. Mao, Z. Chen, D. Gao, C. Wei, W. Zhang, G. Yu, *Chem. Mater.* **2016**, 28, 2209; b) W. Yue, M. Nikolka, M. Xiao, A. Sadhanala, C. B. Nielsen, A. J. P. White, H.-Y. Chen, A. Onwubiko, H. Sirringhaus, I. McCulloch, *J. Mater. Chem. C* **2016**, 4, 9704; c) C. Wei, W. Zhang, J. Huang, H. Li, Y. Zhou, G. Yu, *Macromolecules* **2019**, 52, 2911; d) G. Zhang, H. Yu, Y. Sun, W. Wang, Y. Zhao, L. Wang, L. Qiu, Y. Ding, *J. Mater. Chem. C* **2021**, 9, 633.
[14] R. Sriram, C. N. Sessa Sai Pavan Kumar, N. Raghunandan, V. Ramesh, M. Sarangapani, V. J. Rao, *Synth. Commun.* **2012**, 42, 3419.
[15] H. Hwang, D. Khim, J.-M. Yun, E. Jung, S.-Y. Jang, Y. H. Jang, Y.-Y. Noh, D.-Y. Kim, *Adv. Funct. Mater.* **2015**, 25, 1146.
[16] Q. Liu, S. Kumagai, S. Manzhos, Y. Chen, I. Angunawela, M. M. Nahid, K. Feron, S. E. Bottle, J. Bell, H. Ade, J. Takeya, P. Sonar, *Adv. Funct. Mater.* **2020**, 30, 2000489.
[17] S. Wood, J. R. Hollis, J.-S. Kim, *J. Phys. D Appl. Phys.* **2017**, 50, 073001.
[18] P. M. Burrezo, J. L. Zafra, J. T. López Navarrete, J. Casado, *Angew. Chem., Int. Ed.* **2017**, 56, 2250.

- [19] Z.-Y. Wang, Y.-Z. Dai, L. Ding, B.-W. Dong, S.-D. Jiang, J.-Y. Wang, J. Pei, *Angew. Chem., Int. Ed.* **2021**, 60, 4594.
- [20] B. Dellinger, S. Lomnicki, L. Khachatryan, Z. Maskos, R. W. Hall, J. Adoukpe, C. McFerrin, H. Truong, *Proc. Combust. Inst.* **2007**, 31, 521.
- [21] C. Wentrup, M. J. Regimbald-Krnel, D. Müller, P. Comba, *Angew. Chem., Int. Ed.* **2016**, 55, 14600.
- [22] G. Zhang, Y. Zhao, B. Kang, S. Park, J. Ruan, H. Lu, L. Qiu, Y. Ding, K. Cho, *Chem. Mater.* **2019**, 31, 2027.
- [23] a) V. S. Bryantsev, V. Giordani, W. Walker, M. Blanco, S. Zecevic, K. Sasaki, J. Uddin, D. Addison, G. V. Chase, *J. Phys. Chem. A* **2011**, 115, 12399; b) H. Qi, Y.-H. Chen, C.-H. Cheng, A. J. Bard, *J. Am. Chem. Soc.* **2013**, 135, 9041.
- [24] a) M. E. Ziffer, S. B. Jo, Y. Liu, H. Zhong, J. C. Mohammed, J. S. Harrison, A. K. Y. Jen, D. S. Ginger, *J. Phys. Chem. C* **2018**, 122, 18860; b) M. Kim, W.-T. Park, S. A. Park, C. W. Park, S. U. Ryu, D. H. Lee, Y.-Y. Noh, T. Park, *Adv. Funct. Mater.* **2019**, 29, 1805994.
- [25] a) Y. Zhou, C. Fuentes-Hernandez, J. Shim, J. Meyer, A. J. Giordano, H. Li, P. Winget, T. Papadopoulos, H. Cheun, J. Kim, M. Fenoll, A. Dindar, W. Haske, E. Najafabadi, T. M. Khan, H. Sojoudi, S. Barlow, S. Graham, J.-L. Brédas, S. R. Marder, A. Kahn, B. Kippelen, *Science* **2012**, 336, 327; b) C. Liu, Y. Xu, Y.-Y. Noh, *Mater. Today* **2015**, 18, 79; c) J. Bai, Y. Jiang, Z. Wang, Y. Sui, Y. Deng, Y. Han, Y. Geng, *Adv. Electron. Mater.* **2020**, 6, 1901002.
- [26] D. X. Long, E.-Y. Choi, Y.-Y. Noh, *Dyes Pigm.* **2017**, 142, 323.